Terahertz probing of sunflower leaf multilayer organization

Yannick Abautret* [1], Dominique Coquillat [2], Myriam Zerrad[1], Xavier Buet[1], Ryad Bendoula [3], Gabriel Soriano [1], Nicolas Brouilly [4] Daphné Héran[3], Bruno Grèzes-Besset [5], Frédéric Chazallet [6] and Claude Amra [1]

[1]*Aix Marseille Univ, CNRS, Centrale Marseille, Institut Fresnel, Faculté des Sciences - Campus Saint Jérôme, Avenue Escadrille Normandie-Niemen, 13397 Marseille, France*
[2]*Laboratoire Charles Coulomb (L2C), Université de Montpellier, CNRS, Montpellier, France*
[3]*ITAP, INRAE, Montpellier SupAgro, Univ. Monptellier, Monptellier, France*
[4]*Aix Marseille University, CNRS, IBDM, 13288 Marseille*
[5]*Innolea, 6 chemin des Panedautes, 31700 Mondonville, France*
[6]*Shakti, 45 Rue Frédéric Joliot-Curie, 13013 Marseille, France*
yannick.abautret@fresnel.fr

Abstract: We analyze the multilayer structure of sunflower leaves from Terahertz (THz) data measured in the time-domain at a ps scale. Thin film Reverse Engineering Technique (RET) are applied to the Fourier amplitude of the reflected and transmitted signals in the frequency range $f < 1.5$ THz. Validation is first performed with success on etalon samples. The optimal structure of the leaf is found to be a 8-layer stack, in good agreement with microscopy investigations. Results may open the door to a complementary classification of leaves.

© 2020 Optical Society of America under the terms of the OSA Open Access Publishing Agreement

1. Introduction

Over the past decades, climate change has challenged agronomist to find new techniques and plant varieties genetically adapted to water stress. Indeed, lack of water and drought episodes that threaten several regions of the world in the close future have increased the number of scientific investigations on new phenotyping tools and techniques. Until now, phenotyping has required statistical analysis with a huge number of data to measure and process. In this context, the availability of massive characterization vectors, like phenotyping platforms, offers new opportunities for the development of optical investigation tools. For example, multi-spectral and infrared imaging are already operational at the level of the crop [1,2].

In this new context, there is also a growing demand to develop non-contact (optics, acoustics, mechanics...) techniques to analyze leaves microstructure. Among them are optical techniques that have been used for decades to probe elastic and non-elastic properties of the plants [3]. Luminescence properties were extensively explored and mainly provide chemical information (chlorophyll-related) about the samples and photosynthesis [4–6], while few information concerns the opto-geometrical properties, that is, the thicknesses and indices of the layers which constitute the leaf. Optical coherence tomography (OCT) is another modern technique which allows to probe the thickness of the sample and may allow to emphasize the multilayer structure [7]. However, the depth probe is often limited around 50 μm, a value which may be decreased depending on the leaf heterogeneities responsible for high scattering that is plant-dependent.

More classical are the spectro-photometric techniques though they have today led to the development of hyperspectral imaging systems. Relevant information [8,9] is collected with these systems but they do not provide accurate data about the opto-geometrical parameters of the leaf. Indeed, the leaf structure gathers rough interfaces and inhomogeneous bulks which totally scatter the incident light and loose the coherence properties of light; the resulting speckle pattern

is complex (see [10]) and does not allow to retrieve the information about the multilayer structure, even when exact electromagnetic theories are used.

In order to solve this last point (related to the complexity of the speckle pattern created by leaf heterogeneities), one basic idea consists in increasing the wavelength (λ) of light. Indeed we know that the weight of the inhomogeneities decreases at large wavelengths, and that the optical resolution is given by the probing wavelength. Surface light scattering for instance would be strongly reduced for low roughness-to-wavelength ratios (δ/λ), with δ the root-mean-square of the leaf roughness. Since roughness measurements obtained with white light interferometry microscopy indicate that δ is of the order of a few micro-meters, a wavelength in the mm range would guarantee that most of the reflected or the transmitted energies is carried by the specular beams, that is, in the directions of Snell/Descartes law. This is the reason why this work is focused on a THz investigation of leaves. As the result of negligible scattering in the THz frequency-range, the leaf structure is seen by the THz system as a quasi-planar homogeneous multilayer, and this allows to use most techniques of the optical thin film [11] (optical coatings) community to retrieve the opto-geometrical parameters (the organization) of the leaf from spectral data. Roughly speaking, for single layers these techniques take full advantage of the location of extrema that can be seen in the wavelength variations of reflection and transmission, and of the contrast between these extrema. For more complex organizations, a specific RET is required.

To summarize, thin film RET is used in this paper to analyse the leaf multilayer through THz pulsed spectroscopy data measured by reflection and transmission. By comparison with optical thin film techniques, we must stress on a number of key differences (in addition to the different wavelength ranges and associated technologies for emitters, detectors and components in the optics and THz regimes). The first difference is related to the high absorption level of plants in specific spectral regions (which are mainly due to water and pigments), which does not exist in high precision multi-dielectric coatings; such difference will give more complexity to the inverse problem to solve in leaves. The second difference is connected with the nature (temporal or spectral) of the source; indeed, while broad-band CW sources are currently used in optics, this is not the case for THz sources, for which reason broad-band THz sources most often work in a temporal (pulsed) regime. Though the theory is the same if we use the time-frequency equivalence, this will require to discuss and adjust a number of numerical procedures.

This paper presents in section 2 the THz technics and main caracteristics used for this study. A validation campaign on samples is performed and depicted in section 3. Once the validation step is done, the study focuses on the sunflower leaf sample in section 4. Finally, results and perspectives of this work are summarized in section 5.

2. THz Time-Domain Spectroscopy (TDS)

THz spectroscopy is today largely used to probe films of inert materials whose thickness is of the order of 1mm [12, 13]. The measurement techniques are similar to those of optics, that is, the thickness and index of the film are derived from the reflection or transmission data.

In the field of agronomy, TDS was used to analyze and monitor the water content status of plants by measuring transmission. Water is a very absorbing material in THz-domain and this property has been used to evaluate water content and the physiologic behavior of plants during water stress situation [14–16]. Correlation between water content and transmission level has been established and these results offer a new way to develop a non-invasive and faster tool to measure water plant status.

2.1. Experimental set-up

In this study we performed the measurements campaign on a Terapulse 4000 spectrometer with external sample chamber compatible with a specular reflectance and transmission module (TeraView Ltd., Cambridge, UK). THz radiation is produced by ultra-short pulse fibre laser

(wavelength 790 nm, pulse duration <100 fs). The pulse is separated into a pump and probe beam, where the pump beam generates THz radiation and the probe beam detects THz pulses using laser-gated photoconductive emitters and detectors. The incident THz pulse was sampled with a spacing of the data points in the time-domain Δt of 0.02 ps over an optical delay extend of 1000 ps, enabling a high spectral resolution of 1.0 GHz. Spectra were the average of 100 scans (approximately 10-min measuring time). Parabolic mirrors focus the THz radiation onto the sample and the set-up can be used in transmission mode or in reflection mode. The sample compartment can be nitrogen-purged to make sure that no residual water vapour peaks are visible in the spectra.

Notice that, as a non-destructive and non-invasive technique, THz TDS does not require sample preparation. Thus the samples under investigation were directly placed on the sample holder which is an aluminum disk with a 2-cm-diameter-hole at the center. The interested region of the leaf, placed in the middle of the disk, is maintained steady in an average plane. Concerning the leaves, the upper epidermis was facing the incoming THz pulse. More details about THz technology can be found in numerous papers such as [17].

2.2. Calibration

Let us denote by $e(\tau)$ the THz pulse incident on the sample, and by $s(\tau)$ the signal delivered by the leaf under illumination. Assuming a linear interaction, the input/output relationship can be written as:

$$s(\tau) = e(\tau) * h(\tau) \tag{1}$$

Where $(*)$ designates a convolution product over time τ, and $h(\tau)$ the impulse response (or transfer function) of the sample under study. This impulse response is characteristic of a linear filter and takes into account of the inertia of the leaf tissues. It carries the information which is leaf-related. Note that inertia is absorption-related and takes account of the dispersion of the complex indices of the leaf.

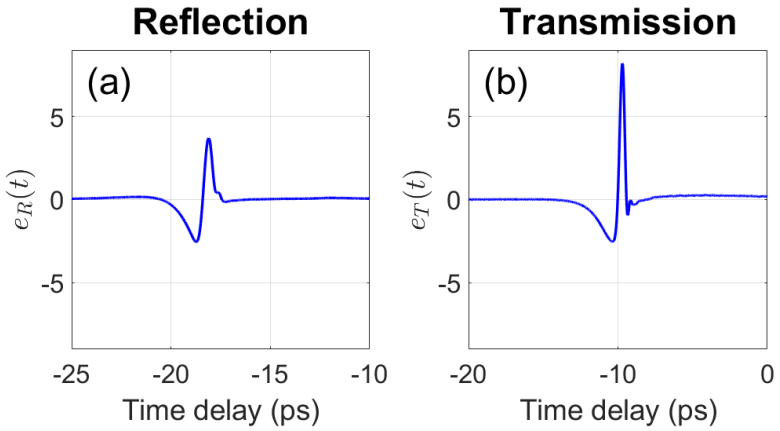


Fig. 1. Input signals delivered in the absence of sample, (a) for reflection and (b) transmission modes. Signal in reflection has been acquired thanks to a gold mirror.

Reflection and transmission measurements require different set-up geometries. For that reason it is necessary to measure $e(\tau)$ in both configurations (reflection and transmission modes) and we will note the two incident pulses as $e_R(\tau)$ and $e_T(\tau)$ before leaf interaction. We precise here that reference in reflection is taken with a sample of a gold sheet which is equivalent to a mirror

in the optical range. Hence, according to the mode under study, the leaf signal is written as:

$$s_R(\tau) = e_R(\tau) * h_R(\tau) \tag{2}$$

$$s_T(\tau) = e_T(\tau) * h_T(\tau) \tag{3}$$

where $h_R(\tau)$ and $h_T(\tau)$ are considered for reflection and transmission data. Actually they are connected with the inverse Fourier transforms of the amplitude reflection $r(\omega)$ and transmission $t(\omega)$ coefficients currently measured in the Fourier space in optics.

The two measured (input) signals $e_R(\tau)$ and $e_T(\tau)$ are plotted in Fig. 1(a) and 1(b) in a 15 ps time interval. These curves are the signals delivered by the detector in response to the incident THz pulse in reflection and transmission modes in the absence of the leaf. The difference in these curves is attributed to the difference in the configuration modes. Their characterization is therefore necessary in the calibration process.

2.3. Fourier spectrum of the reference signals

Since RET will be performed in the Fourier space, it is interesting at this step to analyse the Fourier spectrum of the input signals. These spectra are given in Fig. 2 at frequencies below 5 THz. We observe the presence of noise at high frequencies ($f > 3$ THz), for which reason RET will be limited to the frequency window ($f < 3$ THz) of meaningful data.

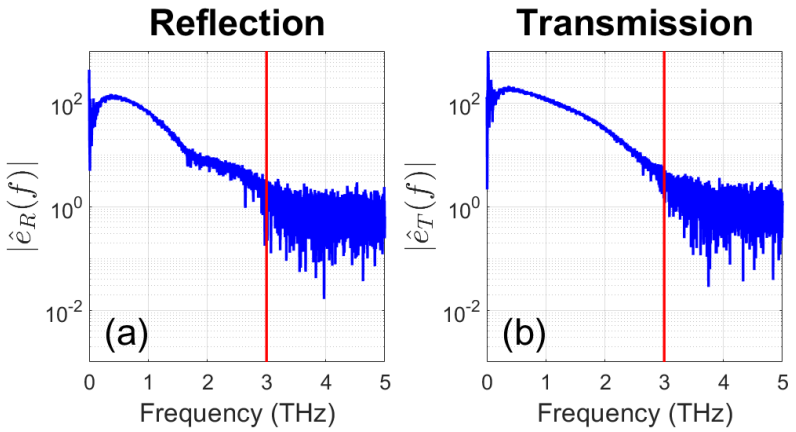
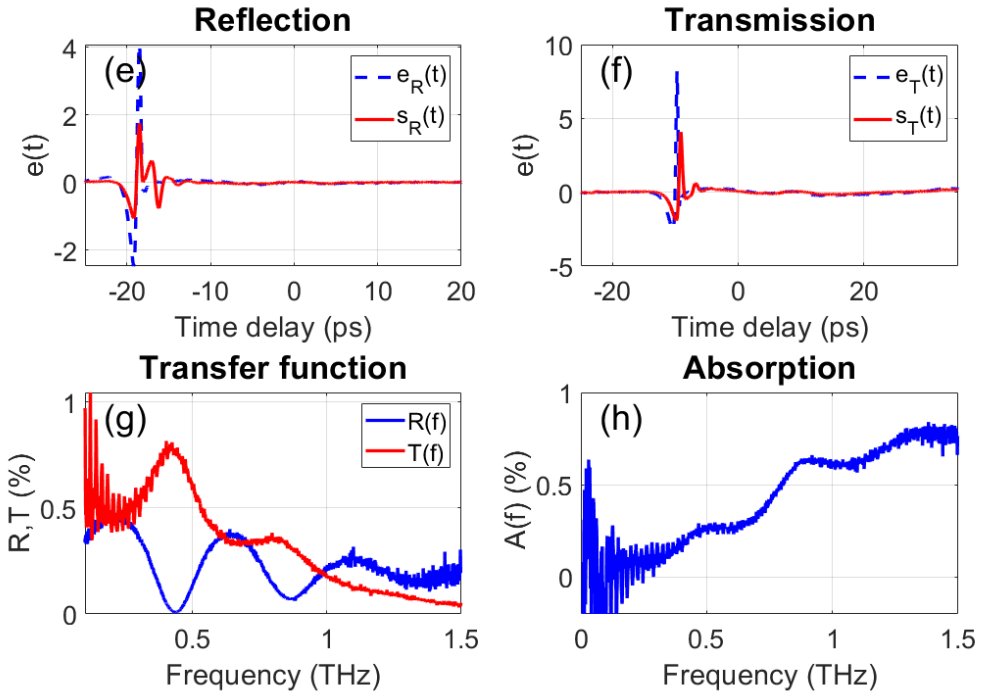


Fig. 2. Frequency-domain projection of incident beam (a) in the reflection mode $\hat{e}_R(f)$ and (b) transmission mode $\hat{e}_T(f)$.

3. Etalon samples

Before proceeding to the leaf analysis, it is prudent to test the procedure on etalon samples. These 3 reference materials are one Corning microscope slide (provided by SIGMA-ALDRICH ref : CLS294775X50) of thickness in the range 900 to 1100 μm, one Menzel Cover Slip (provided by Thermo Fisher Scientific ref : 24X30-1W-YO) of thickness around 150 μm, and a high-resistivity silicon wafer double slide polished with a thickness around 525 μm (provided by NEYCO). The time-domain signals and their Fourier spectra are given in reflection and transmission modes for these 3 samples in Fig. 3. In these plots, we only consider the frequency range $f < 1.5$ THz due the weak signal-to-noise ratio beyond this limit. Notice here that the Fourier spectra are those of the samples, that is, the transfer functions given by the ouput-to-input ratios of the signals:

$$\hat{h}(f) = \frac{\hat{s}(f)}{\hat{e}(f)} \tag{4}$$



The input signal is also plotted in dotted line for each time-domain curve. This allows to emphasize the different echoes by reflection and transmission, that are related to the thickness and index dispersion of the samples. The higher the thickness, the later the echoes. Depending on the sample parameters, such echoes are easy to observe or not. The sample parameters are also responsible for the quasi-periodic oscillations in the spectrum of the signal. The higher the thickness, the smaller the period. The oscillations should contain absorption information due to finger-prints of the chemical substances. However, these finger-prints are negligable in our case for the frequency range $f < 1.5$ THz. This oscillation vanishes at high frequencies for the first two samples, due to absorption. Note in the Fourier space that we plotted the square modulus of the transfer function, that is:

$$\left|\hat{h}_R(f)\right|^2 \quad \text{and} \quad \left|\hat{h}_T(f)\right|^2 \tag{5}$$

Also, the absorption is taken as:

$$A = 1 - \left(\left|\hat{h}_R(f)\right|^2 + \left|\hat{h}_T(f)\right|^2\right) \tag{6}$$

We notice that the high-resistivity silicon wafer sample has a negligible absorption in the whole frequency range f < 1.5 THz. This can be seen by the repeated zero values taken by reflection at specific frequencies. Indeed at these frequencies the sample is a multiple half- wave layer between 2 identical surrounding media, so that reflection cancels in the absence of absorption (the transparent half-wave layer is known to be absentee). Hence, it would be useless to measure transmission since we can deduce it by T = 1-R. We also notice the presence of noise in the vicinity of the zero frequency, whose origins are not clearly identified at this step (the values approach the mean value of the time signal and this could require a lower time sampling).

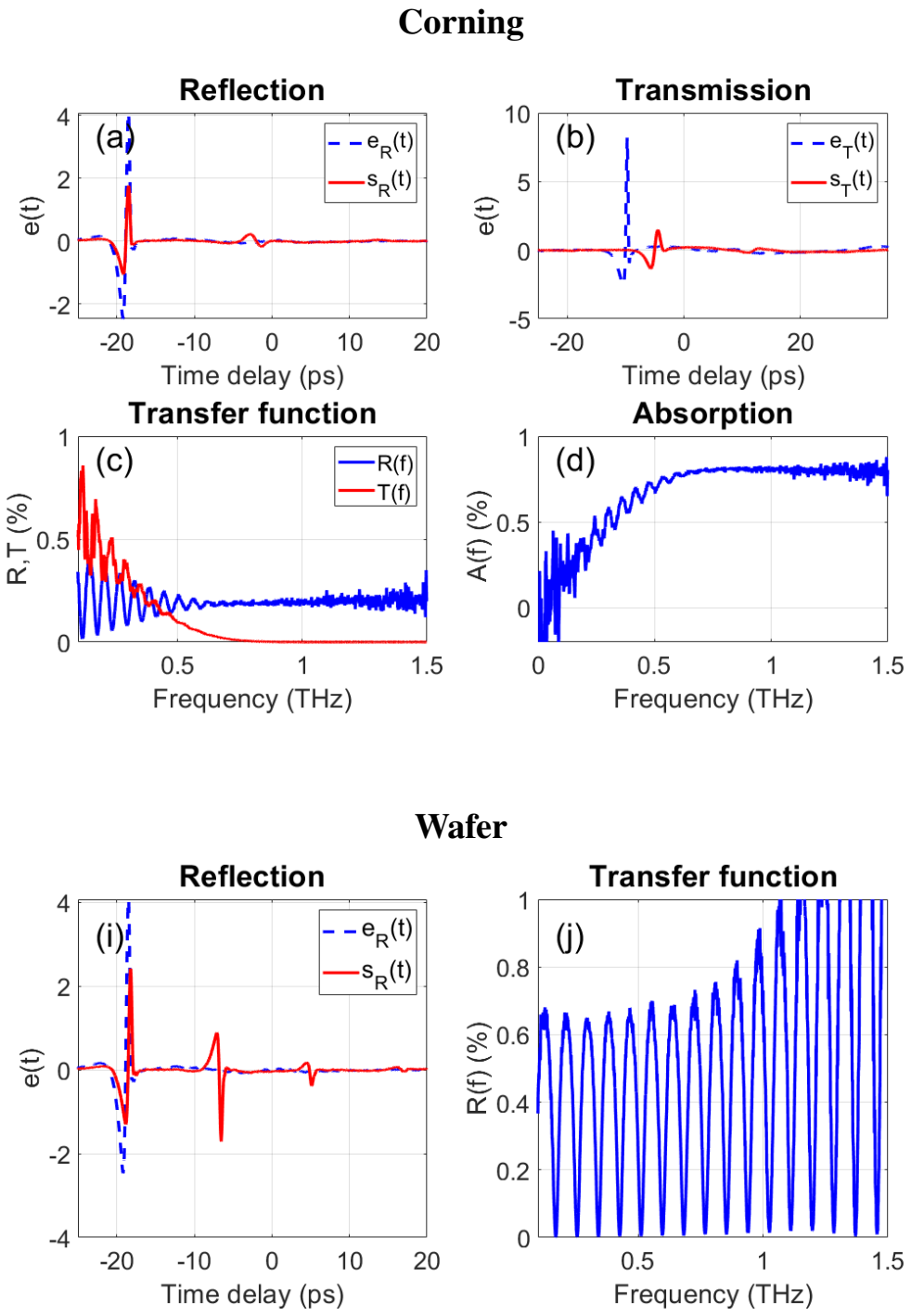


Fig. 3. Time signals and Fourier spectra of the 3 etalon samples measured in reflection and transmission modes, (a-d) for Corning Microscope Slide and (e-h) for Menzel Cover Slip sample. For High-resistivity Silicon Wafer, (i) is time-domain signal on reflection mode and (j) its transfer function.

3.1. Transfer function, reflection and transmission coefficients

Here we connect the transfer function to the amplitude reflection and transmission coefficients of the sample. The input pulsed signal is collimated at quasi-normal illumination on the sample. Hence the THz pulse $e(\tau)$ can be written as a collimated frequency wave packet:

$$e(\tau) = \int A(\omega) e^{jk_0(\omega)(z-z_0)} e^{-j\omega\tau} d\omega \tag{7}$$

with z_0 ($z_{0,R}$ or $z_{0,T}$) is related to a phase origin, and where the width $\Delta\omega$ of the amplitude distribution $A(\omega)$ is the inverse of the pulse duration. The parameter k follows $k_0(\omega) = \omega n_0/c = 2\pi n_0/\lambda$, with c the speed of light in vacuum, λ the illumination wavelength in vacuum and n_0 the refractive index of the incident medium. Most often, except in vegetal domain where water is majority, this index dispersion is negligible, which leads to:

$$e(\tau) = \check{A}[\tau - (\frac{n}{c})(z - z_0)] = \check{A}(\tau) * \delta[\tau - (\frac{n}{c})(z - z_0)] \tag{8}$$

with $\check{A}(\tau)$ the inverse Fourier transform of $A(\omega)$ and δ the Dirac distribution.

The transmitted field is given by a formula similar to (8) but in which the amplitude distribution is weighted at each frequency by the transmission coefficient $t(\omega)$ of the leaf, that is:

$$s_T(\tau) = \int t(\omega) A(\omega) e^{jk_0(\omega)(z-z_{0,T})} e^{-j\omega\tau} d\omega \tag{9}$$

This yields:

$$s_T(\tau) = \check{t}(\tau) * \check{A}(\tau) * \delta[\tau - \frac{n}{c}(z - z_{0,T})] \tag{10}$$

with $\check{t}(\tau)$ the inverse Fourier transform of the transmission coefficient $t(\omega)$. The result is analogous for the reflected field, that is:

$$s_R(\tau) = \check{r}(\tau) * \check{A}(\tau) * \delta[\tau - \frac{n}{c}(z - z_{0,R})] \tag{11}$$

Relations (10) and (11) show that the transfer functions are identified to the inverse Fourier transforms of the reflection and transmission coefficients:

$$h_T(\tau) = \check{h_T}\left[\tau - \frac{n}{c}(z_0 - z_T)\right] \Leftrightarrow \widetilde{h_T}(\omega) = t(\omega) e^{\left[-j\omega\frac{n}{c}(z_0 - z_T)\right]} \tag{12}$$

$$h_R(\tau) = \check{h_R}\left[\tau - \frac{n}{c}(z_0 - z_R)\right] \Leftrightarrow \widetilde{h_R}(\omega) = r(\omega) e^{\left[-j\omega\frac{n}{c}(z_0 - z_R)\right]} \tag{13}$$

and finally:

$$|h_T(f)|^2 = |r(f)|^2 = T(f) \tag{14}$$

$$|h_R(f)|^2 = |t(f)|^2 = R(f) \tag{15}$$

These last intensity quantities (14) and (15) can be easily measured whatever the position of detectors by reflection and transmission, and on which reverse engineering techniques can be applied. Note also that RET can be applied on the amplitude quantities, (12) and (13), but the difference $z_0 - z_R$ and $z_0 - z_T$ should be perfectly controlled. Indeed they create in the Fourier space an additional residual phase term which can be written as:

$$\varphi_{res} = \frac{2\pi f}{c} n \Delta z \tag{16}$$

For this phase term to be negligible, we must have $\varphi_{res} \ll 2\pi$, that is:

$$\frac{2\pi f}{c} n\Delta z \ll 2\pi \Rightarrow \Delta z \ll \frac{c}{f} \quad \text{with} \quad n = 1 \tag{17}$$

Since the maximum frequency is 1.5 THz, we obtain $\Delta z \ll 200\ \mu$m. To summarize, this last condition should be satisfied when working with the amplitude coefficients rather than with the intensity coefficients.

3.2. Non dispersive analysis of the samples

In the Fourier space multiple reflections at each interface of a single layer classically allow to write the amplitude reflection and transmission coefficients of the layer as:

$$r(\omega) = r_0 + t_0 t_0' r_1 \sum_q (r_0' r_1)^q e^{2j(q+1)\varphi} \tag{18}$$

$$t(\omega) = t_0 t_1 \sum_q (r_0' r_1)^q e^{j(2q+1)\varphi} \tag{19}$$

with r_i and t_i the Fresnel coefficients of interface (i) between media i (incident) and $i+1$, while r_i', t_i' are the same coefficients when the illumination is reversed. The phase term is given by:

$$\varphi = \alpha e, \quad \text{with} \quad \alpha = (k_1^2 - \sigma^2)^{\frac{1}{2}} \quad \text{and} \quad k_i = \frac{2\pi n_i}{\lambda} \tag{20}$$

with λ the illumination wavelength in vacuum, n_1 the complex index of the layer and e its thickness. The spatial pulsation σ is given by : $\sigma = k_0 sin\theta_0$ with θ_0 the illumination incidence angle. Note here that the substrate is air ($n_2 = n_0 = 1$).

In formulae (18) and (19) if we assume negligible absorption (real indices n_i) and index dispersion, the frequency dispersion is only hold in the phase term φ, so that the inverse time Fourier transform is immediate at normal illumination ($\alpha = k = \omega n/c$), that is:

$$\check{r}(\tau) = r_0 \delta(\tau) + t_0 t_0' r_1 \sum_q (r_0' r_1)^q \delta[\tau - 2(q+1) n_1 \frac{e}{c}] \tag{21}$$

$$\check{t}(\tau) = t_0 t_1 \sum_q (r_0' r_1)^q \delta[\tau - (2q+1) n_1 \frac{e}{c}] \tag{22}$$

with δ the Dirac function. These last formulae emphasize the time locations of the echoes at instants $\tau_R(n) = 2(n+1)n_1 e/c$ by reflection and $\tau_T(n) = (2n+1)n_1 e/c$ by transmission. Taken into account the fact that the orders of magnitude of the Fresnel transmission (t_i) and reflection (r_i) coefficients are unity and a few percent, respectively, we also observe that the first two echoes by reflection have the same order of magnitude (they are proportional to r_0 and $t_0 t_0' r_1$), which is not the case of the echoes by transmission (proportional to $t_0 t_1$ and $t_0 t_1 r_0' r_1$). For that reason and when possible (depending on the receiver detectivity), one would measure the first echo by transmission, and the first two echoes by reflection.

A first evaluation of the sample optical thickness can be extracted from these time instants in reflection and transmission by measuring time delay peaks :

$$\tau_{q,R} = 2(q+1) n_1 \frac{e}{c} \quad \text{Reflection} \tag{23}$$

$$\tau_{q,T} = (2q+1) n_1 \frac{e}{c} \quad \text{Transmission} \tag{24}$$

For both modes, reflection and transmission, time delays between two peaks q and $q+1$, is equal to:

$$\Delta\tau_{(q,q+1)} = \frac{2 n_1 e}{c} \tag{25}$$

Results are given in Table 1, 2 and 3 where optical thicknesses are extracted for each sample. Note that the agreement is high between values extracted by reflection and transmission. Moreover, the agreement is also high for values extracted from more than 2 echoes (case of silicon wafer sample).

Table 1. Time delays of the echoes measured by reflection and transmission for Menzel Cover Slip sample with the associated optical thicknesses.

Menzel				
Time delay (ps)	τ_0	τ_1	$\Delta\tau$	$\delta = n_1 e\ (\mu m)$
R	-18.51	-16.09	2.42	363
T	-9.11	-6.71	2.4	360
Average	∅	∅	2.41	362

Table 2. Time delays of the echoes measured by reflection and transmission for Corning Microscope Slide sample with the associated optical thicknesses.

Corning				
Time delay (ps)	τ_0	τ_1	$\Delta\tau$	$\delta = n_1 e\ (\mu m)$
R	-18.47	-1.43	17.04	2556
T	-4.41	12.63	17.04	2556
Average	∅	∅	17.04	2556

Table 3. Time delays of the echoes measured by reflection and transmission for High resistivity silicon Wafer sample with the associated optical thicknesses.

Wafer				
Time delay (ps)	τ_0	τ_1	τ_2	τ_3
R	-18.21	-6.53	5.09	17.03
Time delay (ps)	$<\Delta\tau>$	$n_1 e\ (\mu m)$		
R	11.81	1772		

However, from these data, we only evaluated the optical thickness of each sample. In order to compare the results to the thickness values of the provider, we have to know the value of the refractive index, which is addressed in the next 2 sub-sections.

3.3. Dispersion estimation of refractive index

Though neglected until now, a few information can also be emphasized about the index dispersion. Indeed, minima of the reflection spectrum correspond to optical thicknesses related to a half

wavelength in the form:

$$n_q e = q\frac{\lambda_q}{2} \quad \text{or} \quad n_q e = \frac{q}{2}\frac{c}{f_q} \tag{26}$$

with f_q the location of the q^{th} minimum of the reflection curve $R(f)$ and e the thickness of the sample. Actually in the frequency-domain and following the optical thicknesses given in Table 1, q starts at 1 with the first minimum of the $R(f)$. From this consideration we can define and evaluate the variation rate of the index $\Delta n_q/n_q = (n_{q+1} - n_q)/n_q$ as :

$$\frac{\Delta n_q}{n_q} = \frac{c}{2n_q e}\left[q\left(\frac{1}{f_{q+1}} - \frac{1}{f_q}\right) + \frac{1}{f_{q+1}}\right] \tag{27}$$

Finally, after calculus, we obtain:

$$\frac{\Delta n_q}{n_q} = \frac{f_q}{f_{q+1}}\left(\frac{q+1}{q}\right) - 1 \tag{28}$$

Results are depicted in Table 4, 5 and 6 and show for the three samples that the dispersion of the real index is negligible (lower than 3%).

Table 4. Dispersion of the real indices for the Menzel Cover Slip etalon, measured between successive wavelengths of minimum reflection.

Menzel			
$f_q(THz)$	0.44	0.87	1.32
$\Delta n_q/n_q(\%)$	1.15	1.14	∅

Table 5. Dispersion of the real indices for the Corning Microscope Slide etalon, measured between successive wavelengths of minimum reflection.

Corning						
$f_q(THz)$	0.06	0.12	0.18	0.24	0.30	0.36
$\Delta n_q/n_q(\%)$	0.00	0.00	0.00	0.00	0	2.44
$f_q(THz)$	0.41	0.48	0.53	0.60		
$\Delta n_q/n_q(\%)$	2.38	1.89	1.85	∅		

3.4. Refraction index estimation

In a similar way, an estimation of the refractive index can be done with the amplitude of the maxima. Indeed the maxima occur for optical thicknesses in the form:

$$n_q e = (2q+1)\frac{\lambda_q}{4} \tag{29}$$

Provided that absorption can be neglected at low frequencies, means large wavelengths, the reflection maxima can be written as:

$$r = \frac{1-n_q^2}{1+n_q^2} \Leftrightarrow R = \left(\frac{1-n_q^2}{1+n_q^2}\right)^2 \tag{30}$$

Table 6. Dispersion of the real indices for the High resistivity silicon Wafer etalon, measured between successive wavelengths of minimum reflection.

Wafer						
$f_q(THz)$	0.08	0.17	0.26	0.34	0.43	0.51
$\Delta n_q/n_q(\%)$	0	1.92	1.96	1.16	1.18	0.83
$f_q(THz)$	0.60	0.68	0.77	0.85	0.94	
$\Delta n_q/n_q(\%)$	0.84	0.65	0.65	0.53	∅	

That is:

$$n_q = \sqrt{\frac{1+\sqrt{R_q}}{1-\sqrt{R_q}}} \tag{31}$$

Table 7. Refraction index and thickness values extracted at frequencies of maximum reflection.

Sample	1^{st} max (THz)	R (%)	n	$e(\mu m)$	ne
Menzel	0.21	48	2.34	155	$0.36.10^{-3}$
Corning	0.09	48	2.34	1092	$2.56.10^{-3}$
Wafer	0.13	71	3.42	518	$1.77.10^{-3}$

Notice that absorption at low frequencies or large wavelengths can be approximated by:

$$\frac{e}{\lambda} \ll 1 \Rightarrow A \approx \mid 1+r \mid^2 \omega\varepsilon'' \frac{e}{2} \tag{32}$$

with $\omega = 2\pi f$ and ε'' is the imaginary part of the permittivity. This relation shows why absorption is lower at low frequencies (under the assumption of negligible dispersion), which legitimates the use of (31) to estimate refraction index. Results are given in Table 7 and show realistic values of the real index and associated thickness. For example, if we consider the silicon wafer refractive index as 3.4, we find a thickness of the wafer sample $e \approx 521$ μm. This value is in a very good agreement with manufacturing data since the thickness is announced to be 525 +/- 20 μm.

4. THz organization analysis of the sunflower leaf

4.1. RET

Here, we go further with a RET, a well-known procedure currently used in optical thin films. In regard to the previous sections, note also that absorption is now considered, though dispersion is still neglected.

In this section, the data are analyzed in the Fourier space while we could have chosen to do so in time-domain like some studies already did [18, 19]. For each set of parameters, we define a merit function as the distance between the measurements (r_M, t_M) and the calculation (r_C, t_C)

performed with these parameters, that is :

$$M(n_i, e_i, Q) = \sum_{i=1}^{Q} \{[r_M(f_i) - r_C(f_i)]^2 + [t_M(f_i) - t_C(f_i)]^2\} \tag{33}$$

Notice here that the distance is not normalized. e_i and n_i are respectively the thicknesses and the complex indices of the stack layers, while Q is the number of frequencies.

As it is shown in Fig. 4, each layer is associated with 3 different parameters which are thickness e_i, and the two parameters of the complex refractive index $n_i + jk_i$. With N layers, the number of parameters is $3N$ if index dispersion can be neglected.

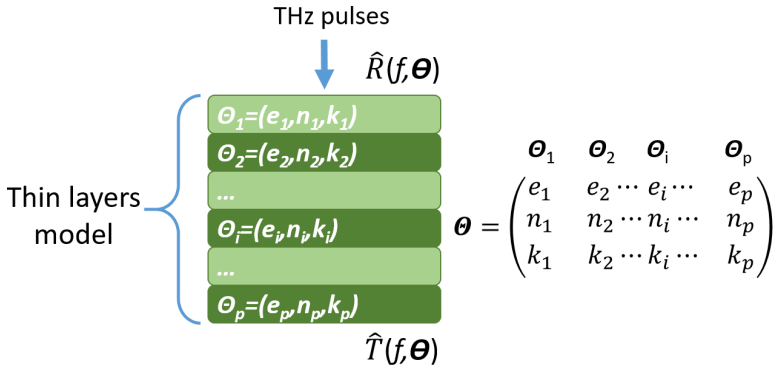


Fig. 4. Modelisation of a p-layer stack. θ is a gathering matrix of the $3p$ parameters.

4.2. *Results on etalon samples*

The algorithm was first tested on the 3 etalon samples we used in section 3.1. Minimization has been done over a range of frequency from 0.1 to 1.5 THz. The parameters (real optical thickness and complex index) which give the lowest merit function for each sample are the following:

$$ne = 1.79\ 10^{-3}\ m \quad \text{and} \quad k = 0 \qquad \text{Silicon Wafer} \tag{34}$$

$$ne = 2.52\ 10^{-3}\ m \quad \text{and} \quad k = 0.09 \qquad \text{Microscope slide} \tag{35}$$

$$ne = 0.34\ 10^{-3}\ m \quad \text{and} \quad k = 0.19 \qquad \text{Cover slip} \tag{36}$$

When compared to those of the preceeding section, we find the following relative differences:

$$\frac{\Delta(ne)}{(ne)} \approx 0.6\% \quad \text{Silicon Wafer} \tag{37}$$

$$\frac{\Delta(ne)}{(ne)} \approx 5.0\% \quad \text{Microscope slide} \tag{38}$$

$$\frac{\Delta(ne)}{(ne)} \approx 6.1\% \quad \text{Cover slip} \tag{39}$$

These results are rather successfull and the slight differences can be attributed to absorption which was not considered in the previous section. The corresponding signals by reflection in the time and frequency domains are plotted in Figs. 5-7, and show a high agreement between calculation and measurement since the ending value of the normalized merit function (residual error) are lowest than 10% in each case. Hence these first results validate the inverse engineering procedure.

Menzel

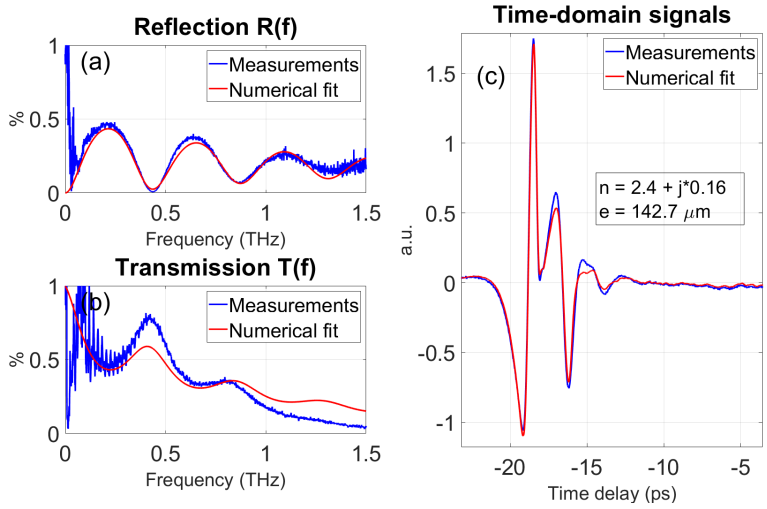


Fig. 5. Numerical fit in frequency-domain on reflection (a) and transmission (b) for $f < 1.5$ THz on the cover slip sample. Reconstruction of the time-domain signal in reflection (c). The measured data are plotted in blue, while the calculation is in red.

Corning

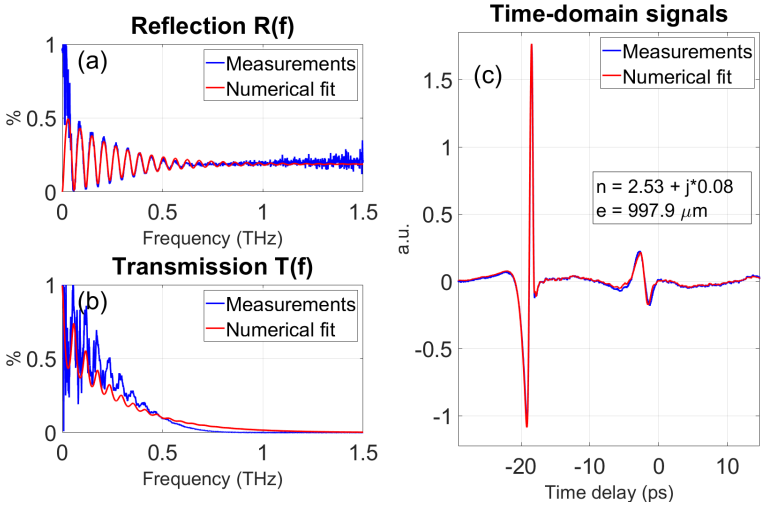


Fig. 6. Numerical fit in frequency-domain on (a) reflection and (b) transmission for $f < 1.5$ THz on the microscope slide sample. Reconstruction of the time-domain signal in (c) reflection. The measured data are plotted in blue, while the calculation is in red.

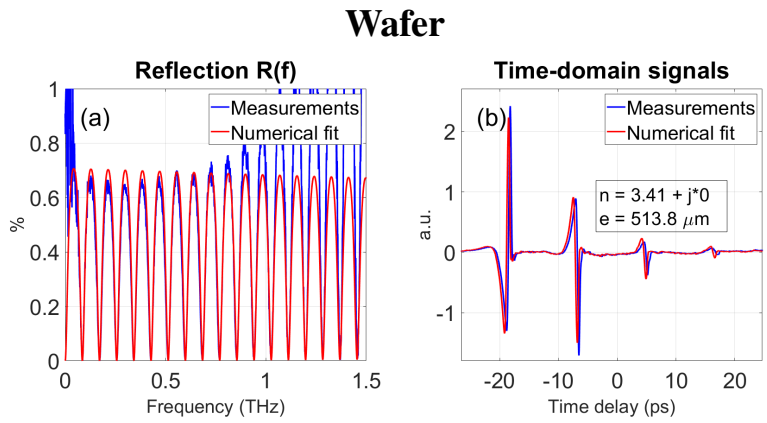


Fig. 7. Numerical fit in frequency-domain on reflection (a) for $f < 1.5$ THz on the silicon Wafer sample. Reconstruction of the time-domain signal in reflection (b). The measured data are plotted in blue, while the calculation is in red.

4.3. Preliminary information on the sunflower leaf

Conversely to living tissues, investigations on vegetal physiology has just started few decades ago but is nowadays a domain largely studied with numerous different aspects. Many works on this topic have been published [20, 21]. For example, photosynthesis mechanisms are clearly identified and understood by biological community as well as stoma functions in temperature and hydration regulation in plants [22]. However, other mechanisms like production of Abscisic acid in leaves or adaptive behaviour in front of different kinds of stress are only partially assimilated. The internal structure of plant leaves is classically described in books [20] but few information can be found about the typical dimensions of their different layers. Thickness, roughness and hairiness of leaves could be a trait that would reveal the way the varieties protect themselves against stresses.

In opposition with the previous cases of single-layer reference samples, the leaf problem is more complex due to the multilayer structure. We will see that eight layers are required to approach the leaf structure. Given this complexity, one cannot deal anymore with multiple reflections at each interface, so that the time echoes and periodic oscillations (when existing in the time and frequency domains) cannot be attributed to a specific interface. Actually the data must be analyzed with the admittance formalism which takes account of the global structure of the stack. Furthermore the assumption of negligible dispersion cannot be justified a priori, so that the number of parameters may be excessive. For that reason preliminary information on the sunflower leaf is crucial before the inverse algorithm is applied on the THz data.

Procedures for scanning electron microscopy (SEM) are quite hard and delicate. For observations of samples have to be water free and covered by a thin conductive layer before being placed onto the sample holder of the system. However plant leaves are living tissues that contain almost 90 percent of water with various internal structures. This means that a simple drying would destroy the leaf organization and lead to useless measurements. Hence, instead of drying the leaf, it is necessary to fix the cell structure and substitute the water by an organic product such as osmium tetroxide OsO4. These two steps are very delicate and take several hours because of the fragile character of the leaves and their complex structures. Eventually a nanometer-thin gold layer is sprayed over the sample to allow electric interaction so that secondary electrons can be produced and detected [23]. The resulting sample is then ready for the SEM analysis and the results are given in Fig. 8.

As expected, the leaf structure reveals strong heterogeneities but the structure can still be

glimpsed. In fact, the protocol has roughly maintained the organization of the leaf together with part of the cells shape. The high-resolution picture emphasizes a specific elongated shape of the palisade mesophyll cells, and the multilayer organization. According to this SEM investigation, and though the protocol has largely reduced the typical dimensions and destroyed part of the inner structure, the sunflower leaf can roughly be described as a 4 layer stack organization, that is: the two upper and lower epidermis layers and the largest mesophyll ones which are called palisade mesophyll and spongy mesophyll. Both of them contain water and chlorophyll pigment but have not the same function. Palisade mesophyll presents a well-organized elongated cells which collect light, use it to photosynthesis reaction and guide it toward lower layers. Spongy mesophyll is composed by cells with different shapes and sizes completely desorganised and unsticked at each other. This typicall organization in spongy mesophyll permits gazes to move. Actually, thickness of palisade layer is about 2 times thinner than spongy one.

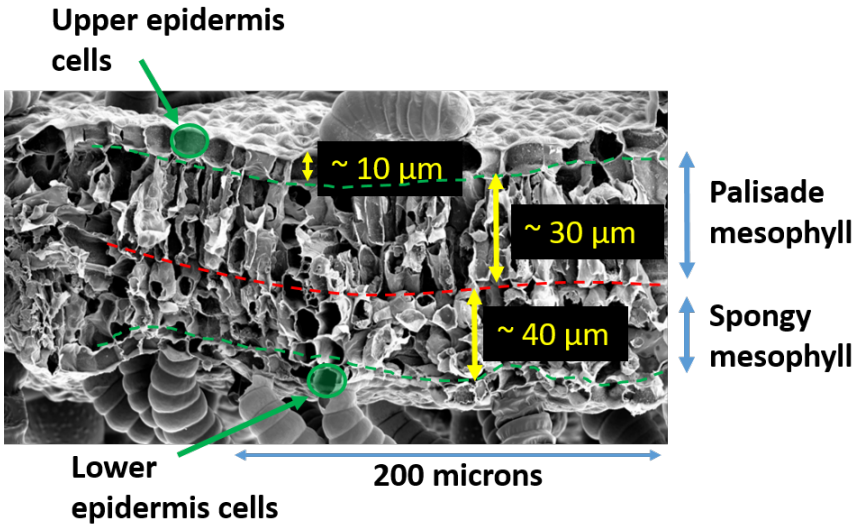


Fig. 8. Scanning electron micrograph of the sunflower leaf cross-section showing a 4 layers stack organization.

Though the conclusions drawn from Fig. 8 cannot serve as a reliable basis for the leaf investigation, they give a first idea of the leaf heterogeneities responsible for the failure of optical techniques (due to complex speckle patterns). Also, they emphasize the symmetry properties within the multilayer structure of the sunflower sample, a symmetry that we use for RET in section 4.5. Eventually at this step we keep in mind that the thicknesses have been reduced by the preparation process and that more layers are expected to be revealed, as announced by the litterature (see Fig. 9 involving 6 layers). Note also that other techniques (environmental SEM or CryoSEM) could be tried to allow less damage on the samples.

4.4. Protocol for the sunflower leaf

Different sunflower plants (dicotyledonous plants) similar in size were watered regularly and used for the THz experiments. The plants were grown from seeds in green houses room under log-day conditions in single pots. Plants were enlightened with horticultural lamp during 8 hours per day (Fig. 10). Two leaves were cut from the petiole before being placed in the THz system, due to the difficulty to place the entire plant close the THz device. In order to minimize plant water stress, we wrapped up the petiole with a wet cotton. Then, to be measured, the samples

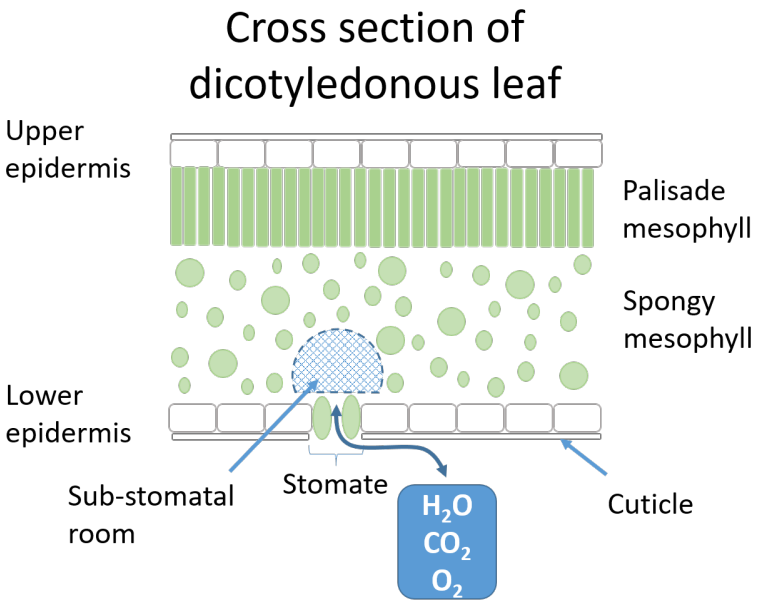


Fig. 9. Expected natural structure of leaf cross-section.

are placed on a metallic sample holder with a hole at the centre. The leaf is delicately stretched and fixed with little magnet to hold the interested zone flat and stable in time. It is necessary to ensure that the measured area does not contain a large rib but only tertiary. These manipulations last about 5 minutes before measurements. The duration of acquisition can varies from 10 to 15 minutes for each acquisition depending on the number of scan we choose.



Fig. 10. Growing chamber of sunflower plants equipped with horticultural lamp, ventilation system and tide tank.

4.5. Reverse engineering on the sunflower leaf

The reflexion THz data on the leaf sample are given in Fig. 11, both in the time and frequency domains.

One key problem is the unicity of the solution, and the time-consuming algorithm. This is why we simplify the problem by considering the leaf structure as a symmetric organization (except

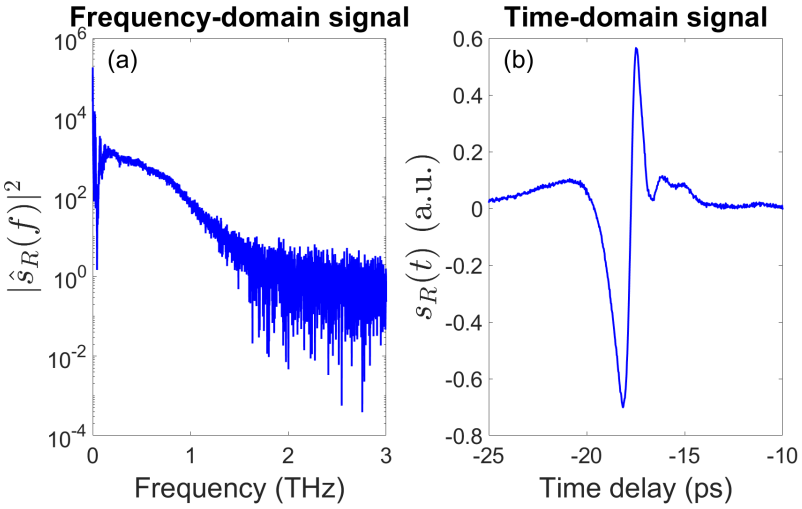


Fig. 11. (a) squared modulus of frequency-domain projection and (b) the reflection signal acquired in time-domain.

mesophyll layers), with an a priori knowledge that was summarized in Fig. 12. Therefore the solutions will be explored in the vicinity of these values. Due to the high number of parameters, we will extract the best solutions (lowest merit functions) for different layer numbers ranging from 1 to 8.

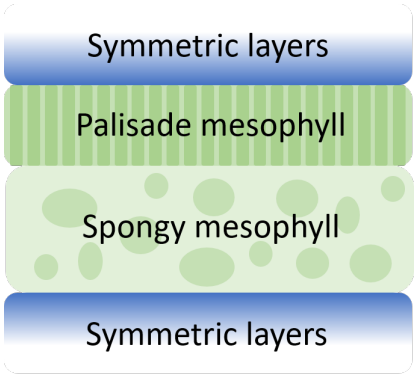


Fig. 12. Symmetry assumptions of the layers for the RET algorythm implemented with Matlab.

We have to face another difficulty in the case of leaves, due to the stationarity of their properties. Indeed when passing from the reflection to the transmission mode, the sample must be removed and replaced and we cannot guarantee that the same surface is illuminated with the required accuracy. In a near future a specific mechanical system will be available to solve this difficulty, but for the moment we are limited to reflection measurements, which reduces the data for RET. However the absence of transmission data can be partially compensated if we work with the amplitude data by reflection (rather than the modulus as done until now) and work with the real and imaginary parts of the reflection spectrum. This is possible because the geometry of the system is not modified between the reference measurement and the reflection measurement, so that the difference $|z_0 - z_R|$ is much lower than 200 μm, which satisfies relation (17). To

summarize, in the case of leaves we will use the RET simultaneously on the real and imaginary part of the reflected spectrum.

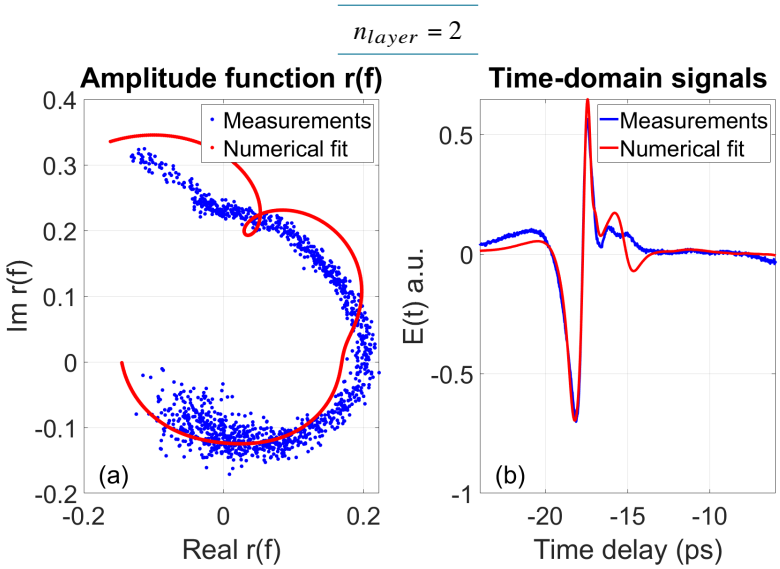


Fig. 13. (a) numerical fit of the Fourier amplitude signal plotted in the complex plane for a 2-layer stack. (b) is a time-domain reconstruction by inverse Fourier transform.

Table 8. Estimated parameters, n, k and e of the two-layer stack model.

$nlayer$	n	k	e (μm)
n_1	1	0.09	91.0
n_2	1.61	0.43	243

Figure 13 is given to show that the sunflower leaf cannot be reduced to a double layer structure. Indeed the best solution is far from the measured data, both in the time and frequency domains. Hence we have to deal with the complexity of the leaf structure and go further with more layers. A good approximation is then reached with 8 layers. With this 8-layer solution (see Fig.14) the two curves (theory and experiment) are quasi-superimposed, and the layer thicknesses of the two mesophyll layers are in agreement with what was expected.

This solution is quite interesting since it allows to recognize the characteristic cross-section of the leaf that was discussed in section 4.3. The two mesophyll layers in the middle of the stack exhibit the expected magnitude orders, with thicknesses equal to $e_4 = 108.1$ μm and $e_5 = 176.3$ μm. Similar results are obtained for the two epidermis layers ($e_3 = 15.3$ μm and $e_6 = 30$ μm) and the two cuticle layers ($e_2 = 3.5$ μm , $e_7 = 1$ μm). Eventually the first and the last layer of the leaf are unexpected, since they exhibit high thicknesses ($e_1 = 76.4$ μm, $e_8 = 134.7$ μm). However their index value is low and this makes us think of the trichomes of the leaf (its hair) whose characteristic dimension is known to vary in the range ($50 - 200$ μm); such trichrome layers are seen here as homogenized layers and this would explain their low index value.

It is important to stress on the fact that the lowest value (18%) of the normalized merit function is reached for layer numbers greater than 6 ($n < 6$). Odd numbers were eliminated because of the symmetry conditions that we forced. Hence the 8 layers solution gives the minimum layer

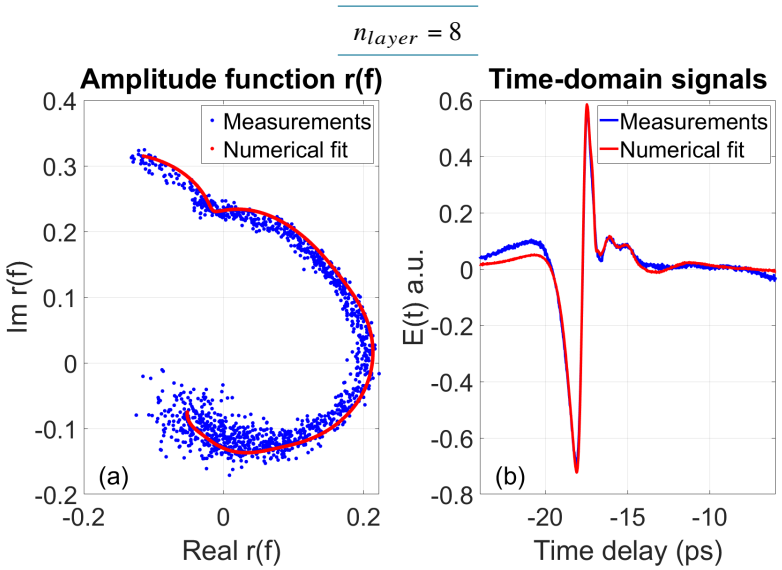


Fig. 14. (a) numerical fit of the Fourier amplitude signal plotted in the complex plane for a 8-layer stack. (b) is a time-domain reconstruction by inverse Fourier transform.

Table 9. Estimated parameters, n, k and e of the eight-layer stack model. The color of the layer 4 and 5 are different since they represent the two mesophyll layers which are not considered symmetrical.

$nlayer$	n	k	e (μm)
n_1	1.03	0	76.4
n_2	1.83	0	3.5
n_3	1.52	0	15.3
n_4	1.79	0.36	108.1
n_5	1.99	0.27	176.3
n_6	1.81	1.05	30.0
n_7	1.6	0.3	1
n_8	1	0.33	134.7

number which minimizes the merit function. Higher even numbers (10 or 12) also give a merit function around 18%, but the layer thicknesses are not realistic since they are all quasi-similar (around 60 micrometers including the cuticle layers) and do not provide a credible representation of the dicotyledonous layer stack.

5. Conclusion

Due to the leaf dimensions (around 500 μm), a THz investigation is well adapted to recover the opto-geometrical multilayer organization of a leaf. Futhermore, these large THz wavelengths reduce all scattering phenomena so that the leaf behaves like a homogeneous multilayer. This balance allowed us to apply the well known (optical thin films) RET to analyze the organization

of a sunflower leaf. Notice however that the reflected and transmitted leaf signals are here measured in the time-domain regime, while they are mostly measured in the frequency-domain in the optical thin film community. These time-domain signals provide the key advantage of an amplitude RET analysis, rather than an intensity one. They were recorded at a ps scale, and their Fourier spectra analyzed in the frequency range f < 1.5 THz.

In a first step our RET techniques were tested and validated with success on 3 etalon single layer inorganic samples. Then they were extended to the analysis of multilayer leaves. The leaf problem is more complex due to the high number of parameters (number of layers, thicknesses and complex indices for each layer, index dispersion). In order to reduce this complexity, the RET thickness solutions were explored in the vicinity of premilinary results issued from SEM microcopy (leaf cross-section). Absorption was considered but dispersion was neglected, thanks to the absence of resonances.

First results clearly show that the leaf organization cannot be reduced to one or 2 layers. A highly realistic solution is reached with 8 layers and allows to recognize the leaf cross-section, including the presence of two mesophyll layers, two epidermis layers, two cuticle layers and two trichrome layers, all of them showing the expected thickness magnitude orders. Notice that the trichrome layers ("leaf hair") lie at the top and the bottom of the leaf and exhibit the higher thicknesses and lower indices, so that they take account of a homogeneization process.

In a near future all results will be improved taking into account, when using the RET technique, the amplitude of both the reflected and transmitted signals on the leaves. This will first allow to approach a unicity in the solution, and then consider complex index dispersion. A specific motorized mechanical system with high positioning accuracy will be required for this application.

All results emphasize the fact that the multilayer leaf structure can be revealed with high accuracy thanks to THz data, and this may open the door to a complementary classification of leaves. In addition, the same investigations can be applied to different kinds of leaf stress, including the water stress.

Funding information

French National Research Agency (ANR-16-CE04-0010)

Acknowledgments

This work was conducted within the OPTIPAG Project supported by the grant ANR-16-CE04-0010 from the French National Research Agency and by the Montpellier University of Excellence I-Site MUSE (PRIME@MUSE), the Région Occitanie, and by the "Gepeto Terahertz platform".

Disclosures

The authors declare no conflicts of interest.

References

1. L. Suárez, P. Zarco-Tejada, G. Sepulcre-Cantó, O. Pérez-Priego, J. Miller, J. Jiménez-Muñoz, and J. Sobrino, "Assessing canopy PRI for water stress detection with diurnal airborne imagery," Remote. Sens. Environ. **112**, 560–575 (2008).
2. A. A. Gitelson, "Remote estimation of canopy chlorophyll content in crops," Geophys. Res. Lett. **32** (2005).
3. Y. Onoda, M. Westoby, P. B. Adler, A. M. F. Choong, F. J. Clissold, J. H. C. Cornelissen, S. Díaz, N. J. Dominy, A. Elgart, L. Enrico, P. V. A. Fine, J. J. Howard, A. Jalili, K. Kitajima, H. Kurokawa, C. McArthur, P. W. Lucas, L. Markesteijn, N. Pérez-Harguindeguy, L. Poorter, L. Richards, L. S. Santiago, E. E. Sosinski, S. A. Van Bael, D. I. Warton, I. J. Wright, S. Joseph Wright, and N. Yamashita, "Global patterns of leaf mechanical properties: Global patterns of leaf mechanical properties," Ecol. Lett. **14**, 301–312 (2011).
4. N. R. Baker, "Applications of chlorophyll fluorescence can improve crop production strategies: an examination of future possibilities," J. Exp. Bot. **55**, 1607–1621 (2004).

5. B. Genty, J.-M. Briantais, and N. R. Baker, "The relationship between the quantum yield of photosynthetic electron transport and quenching of chlorophyll fluorescence," Biochimica et Biophys. Acta (BBA) - Gen. Subj. **990**, 87–92 (1989).
6. E. H. Murchie and T. Lawson, "Chlorophyll fluorescence analysis: a guide to good practice and understanding some new applications," J. Exp. Bot. **64**, 3983–3998 (2013).
7. V. V. Sapozhnikova, V. A. Kamenskii, and R. V. Kuranov, "Visualization of plant tissues by optical coherence tomography," Russ. journal plant physiology **50**, 282–286 (2003).
8. S. Jacquemoud and F. Baret, "PROSPECT: A model of leaf optical properties spectra," Remote. sensing environment **34**, 75–91 (1990).
9. J.-B. Féret, A. Gitelson, S. Noble, and S. Jacquemoud, "PROSPECT-D: Towards modeling leaf optical properties through a complete lifecycle," Remote. Sens. Environ. **193**, 204–215 (2017).
10. A. Ghabbach, M. Zerrad, G. Soriano, S. Liukaityte, and C. Amra, "Depolarization and enpolarization DOP histograms measured for surface and bulk speckle patterns," Opt. express **22**, 21427–21440 (2014).
11. C. Amra, M. Lequime, and M. Zerrad, *Electromagnetic Optics of Thin-Film Coatings: Light Scattering, Giant Field Enhancement, and Planar Microcavities* (Cambridge University Press, 2020).
12. L. Duvillaret, F. Garet, and J.-L. Coutaz, "A reliable method for extraction of material parameters in terahertz time-domain spectroscopy," IEEE J. Sel. Top. Quantum Electron. **2**, 739–746 (1996).
13. L. Duvillaret, F. Garet, and J.-L. Coutaz, "Highly precise determination of optical constants and sample thickness in terahertz time-domain spectroscopy," Appl. Opt. **38**, 409 (1999).
14. P. Nie, F. Qu, L. Lin, T. Dong, Y. He, Y. Shao, and Y. Zhang, "Detection of Water Content in Rapeseed Leaves Using Terahertz Spectroscopy," Sensors. **17**, 2830 (2017).
15. M. Borovkova, M. Khodzitsky, P. Demchenko, O. Cherkasova, A. Popov, and I. Meglinski, "Terahertz time-domain spectroscopy for non-invasive assessment of water content in biological samples," Biomed. Opt. Express **9**, 2266 (2018).
16. L. G. Santesteban, I. Palacios, C. Miranda, J. C. Iriarte, J. B. Royo, and R. Gonzalo, "Terahertz time domain spectroscopy allows contactless monitoring of grapevine water status," Front. Plant Sci. **6** (2015).
17. P. Jepsen, D. Cooke, and M. Koch, "Terahertz spectroscopy and imaging - Modern techniques and applications," Laser & Photon. Rev. **5**, 124–166 (2011).
18. R. Peretti, S. Mitryukovskiy, K. Froberger, M. A. Mebarki, S. Eliet, M. Vanwolleghem, and J.-F. Lampin, "THz-TDS Time-Trace Analysis for the Extraction of Material and Metamaterial Parameters," IEEE Transactions on Terahertz Sci. Technol. **9**, 136–149 (2019). Conference Name: IEEE Transactions on Terahertz Science and Technology.
19. S. Krimi, J. Klier, J. Jonuscheit, G. von Freymann, R. Urbansky, and R. Beigang, "Highly accurate thickness measurement of multi-layered automotive paints using terahertz technology," Appl. Phys. Lett. **109**, 021105 (2016). Publisher: American Institute of Physics.
20. W. G. Hopkins, *Physiologie végétale* (De Boeck Supérieur, 2003).
21. T. N. Buckley, K. A. Mott, T. N. Buckley, and K. A. Mott, *Plant, Cell and Environment*.
22. J. C. Shope, D. Peak, and K. A. Mott, "Stomatal responses to humidity in isolated epidermes," Plant, Cell & Environ. **31**, 1290–1298 (2008).
23. A. K. Pathan, J. Bond, and R. E. Gaskin, "Sample preparation for scanning electron microscopy of plant surfaces—horses for courses," Micron. **39**, 1049–1061 (2008).